Progress In Electromagnetics Research B, Vol. 20, 285–302, 2010

TARGET-AIDED SAR IMAGE INTELLIGENT COMPRESSION

X.-H. Yuan, Z.-D. Zhu, and G. Zhang

College of Information Science and Technology
Nanjing University of Aeronautics and Astronautics
Nanjing 210016, China

Abstract—Intelligent compression is important to image transmission in real time over bandlimited channels for synthetic aperture radar (SAR) payloads deployed on unmanned aerial vehicles (UAV), where target areas are encoded with high fidelity, while background data are encoded with lesser fidelity. A target-aided SAR image intelligent compression (TAIC) system is presented in this paper, which utilizes robust fixed-rate trellis-coded quantization (FRTCQ) to encode target sequences and FRTCQ to encode background sequences. Multiresolution constant false alarm rate (CFAR) detector in wavelet domain using db4 based on the multiscale model of target is embedded. Generic region of interest (ROI) mask is created. In order to achieve better quality of target areas decoded, ROI mask is modified. The improved performance using TAIC system by compressing target chips from training set and testing set in Moving and Stationary Target Acquisition and Recognition (MSTAR) database is demonstrated.

1. INTRODUCTION

Synthetic aperture radar (SAR) payloads deployed on UAV will play an important role in future warfare, because these systems can operate in all weather conditions at any time of day or night and generate images of ground in real time [1]. The military is interested in automatic detecting and recognizing targets from imagery [2–7] to help image analysts perform interpretation. UAV can direct imagery data streams to ground station and image analyst through the use of satellite communications. As sensor resolution increased, more than 1 million pixels/s will be produced by SAR system, but satellite communication

Corresponding author: X.-H. Yuan (cedar@nuaa.edu.cn).

channels to transmit image data from UAV are bandlimited. For example, the commercially available T_1 is only about 1.54×10^6 bit/s. Image data must be compressed on-board, then transmitted to the ground stations analysis by automatic target recognition (ATR) system or by image interpreters to provide critical and timely information to field commanders. Conventional image compression algorithms introduce distortion by coding the entire image uniformly which severely degrades the ATR system's performance, not to mention the perceptual quality of image from analyst [8]. Recent works have been devoted to devising content-based compression algorithm, where target areas are extracted by an external on-board ATR algorithm and encoded at a higher bit rate than background with vector quantization or variable length entropy coding [9, 10]. However, due to the physical limitations of on-board SAR, an efficient automatic target detection algorithm incorporated into encoder is required. Furthermore, both vector quantization and entropy coding are susceptible to channel errors. Bonneau has proposed an intelligent compression algorithm using an embedded automatic target detector in [11], but it works only on simulated SAR image.

To realize extreme compression while maintaining high quality of target area for further analysis, we investigate target-aided SAR image intelligent compression (TAIC) system based on Bonneau's. The research presented in this paper is different from others in three-fold. First, we use all-pass filtering to "lift up" the fixed rate trellis quantization (FRTCQ) performance curve of a broad class of sources to the level of memoryless Gaussian FRTCQ. This method is referred to as robust FRTCQ. Second, unlike the method in [11] where all-pass filtering is implemented on whole-image, we only use robust FRTCQ to encode target sequences, which leads to a much less complex implementation since targets only occupy small parts of SAR image. Third, we determine to use db4 wavelet for the TAIC system. Generic ROI mask is generated according to the lifting steps of inverse wavelet transform. In order to achieve better quality of target areas decoded, we modify the ROI mask.

It is common in practice to take logarithm of image intensity value reducing the high dynamic range compatible with the human visual system and transforming multiplicative noise into additive noise. Log-detected SAR image is concerned in this paper.

2. TARGET-AIDED SAR IMAGE INTELLIGENT COMPRESSION

2.1. System Description

The overall Target-aided SAR image intelligent compression system is shown in Fig. 1. High resolution SAR image is first decomposed into 22 subbands using a 2-D discrete wavelet transform (DWT). A standard 4-level dyadic decomposition is performed, with one additional level of decomposition being performed on the highest frequency component following the first decomposition level. ROI is determined by multiresolution detection algorithm. ROI mask is used to classify the wavelet coefficients in each subband into either a target class or a background class. For each subband, the DWT coefficients corresponding to the same class are grouped into sequences; they are normalized by subtracting their mean and divided by their respective standard deviation. Then target sequences are all-pass filtered being nearly Gaussian distribution to be encoded using FRTCQ, and codebooks are designed in one bit increments from 4 to 8 bits/sample optimized for Gaussian distribution. The background sequences are encoded with FRTCQ directly, and codebooks are designed in one bit increments from 1 to 4 bits/sample optimized for the Laplacian distribution, which we have found reasonable [12]. The side information required to encode consists of the mean of sequences in lowest frequency, standard deviations of all sequences, ROI location, size, and codebook indices. The total side information consists of 408 bits. This corresponds to 0.0249 bpp for a 128×128 image.

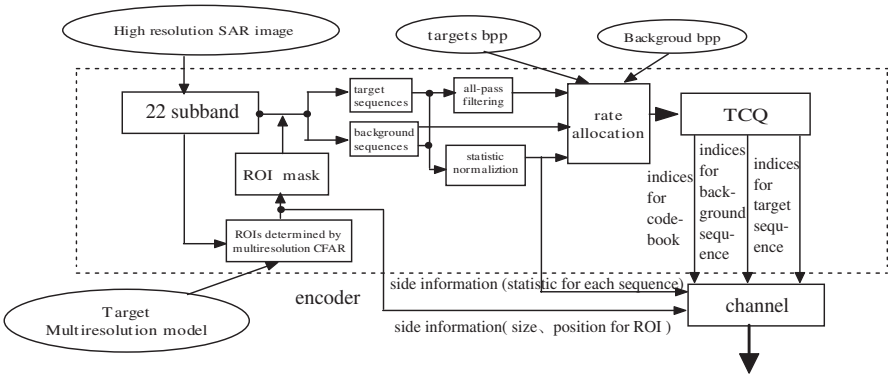

Figure 1. Target-aided SAR image intelligent compression system.

2.2. Robust FRTCQ

Compared with many other quantization schemes, TCQ is moderately robust to channel errors. Fig. 2 shows the obtained signal-to-noise ratio (SNR) of FRTCQ when encoding the memoryless Gaussian, Laplacian, and generalized Gaussian (with shape parameter $\nu = 0.5$) sources at bit rates of 1–4 bits/sample. Also shown are the respective rate-distortion functions (R(D)). From the graph, it is evident that the encoded performance of FRTCQ is opposite to that theoretically possible as seen from the rate distortion functions. To address this issue, a robust quantization method is utilized where the signal to be quantized is all-pass filtered to produce a signal with Gaussian statistics. The all-pass filter is implemented by using a phase scrambling operation. In this way, the performance curves of a Gaussian-optimized quantizer can be achieved with a broad range of source distributions. Thus, a fixed (Gaussian) rate-distortion performance is guaranteed, independent of the source distribution.

To demonstrate the effect of all-pass filtering, Fig. 3 shows the normalized histograms of the Generalized Gaussian ($\nu = 0.5$) 65,535 samples data and phase-scrambling sequence. For comparison, the histogram of same size sample data derived from a Gaussian pseudo-random number generator is also shown. The graph justifies the resulting sequence of phase descrambled generalized Gaussian distribution (GGD) as nearly Gaussian distribution. Note that the variance of the phase-scrambled GGD sequence is identical to the variance of the original GGD sequence due to energy preserve transform [13].

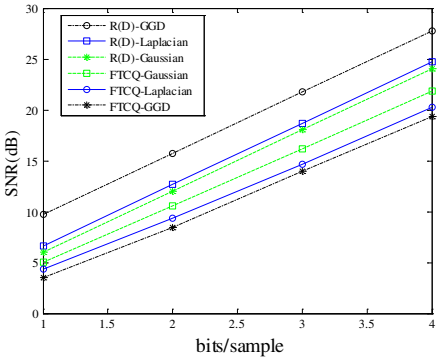

Figure 2. SNR performance of FRTCQ quantization for generalized Gaussian sources.

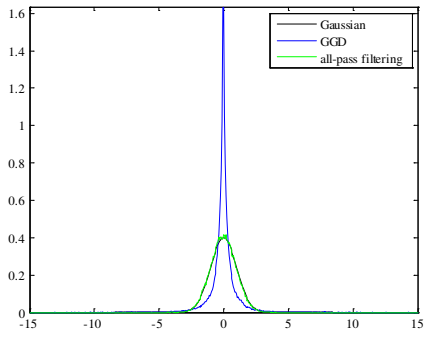

Figure 3. Normalized histogram of GGD (shape parameter $\nu = 0.5$) and phase scrambled sequence.

Table 1. SNR's (dB) of the robust FRTCQ and FRTCQ for memoryless Generalized Gaussian Distribution sources.

	GGD ($\nu = 0.5$)		Gaussian
Rate (bits/sample)	FRTCQ	Robust FRTCQ	FRTCQ
1	3.55	5.02	5.02
2	8.43	10.58	10.54
3	13.98	16.22	16.16
4	19.33	21.94	21.85

The comparison between the resulting SNR performance and those from the non-robust quantizer of GGD source is shown in Table 1. The results of robust quantizer for memeoryless generalized Gaussian source at encoding rates of 1–4 bits/sample are identical to those non-robust quantizer for the memoryless Gaussian source. The same is observed at even higher encoding rates.

Implementing the all-pass filtering using the phase scrambling method can be efficiently done by using fast Fourier transforms (FFT's). An efficient M-point one-dimensional (1-D) FFT requires about $M \log_2 M$ complex multiplications and additions. The size of the FFT's (and inverse FFT) is selected to be the same as that of target sequences. As the target only occupies a small part of image, robust quantization only to target sequences can lead to a much less complex implementation since a relatively few of coefficients need be all-pass filtered.

2.3. Multiresolution CFAR Detection in Wavelet Domain

Conventional compression system contains three building blocks: transform, quantization, and coding. ROI must be extracted before quantization in proposed compression system.

Two-dimensional discrete wavelet transform is applied to a full resolution SAR image, and low frequency subbands $LL_1, LL_2, \ldots, LL_4$ are created. Each of them is normalized by subtracting its mean value forming a multiresolution wavelet coefficient image sequence of $I_1, I_2, \ldots, I_4$. From coarser to finer scales, the wavelet coefficient image values can be predicted by using its coarser-scale ancestor, and scale AR (auto-regressive) models can be written in the form [11].

$$I(s) = a_{1,m(s)} I(s\bar{\gamma}) + a_{2,m(s)} I(s\bar{\gamma}^2) + \ldots + a_{R,m(s)}(s) I(s\bar{\gamma}^R) + w(s) \quad (1)$$

where s has four offspring denoted $s\alpha_{NW}$, $s\alpha_{NE}$, $s\alpha_{SE}$, $s\alpha_{SW}$ and one parent denoted $s\bar{\gamma}$. m denotes scale, and R is the order of the

regression. $m(s)$ is the scale of s, and $a_{1,m(s)}, a_{2,m(s)}, \ldots, a_{R,m(s)}$ are the real, scalar-valued regression coefficients. $w(s)$ is white driving noise.

Defining the vector $\mathbf{a}_k = (a_{1,k}a_{2,k}\ldots a_{R,k})'$, we can characterize a given object (target) in the image first by solving for the autoregressive coefficients, $\mathbf{a}_1$, $\mathbf{a}_2$, ..., and $\mathbf{a}_k$ by least-square approach:

$$\mathbf{a}_k = \arg\min_{\mathbf{a}_k \in R^N} \left\{ \sum_{\{\, s|m(s)=k\}} \left[I(s) - a_{1,k} I(s\bar{\gamma}) - \ldots - a_{R,k} I(s\bar{\gamma}^R) \right]^2 \right\} \quad (2)$$

These regression coefficients are allowed to be scale varying, but restricted to be shift-invariant. The regression length R may be selected in a manner to that standard AR model in time series but limited by the levels of wavelet decomposition.

We can predict the target signal by using these regression coefficients, the residual between the target signal and input is $w(s)$.

$$w(s) = I(s) - \left[a_{1,m(s)} I(s\bar{\gamma}) + \ldots + a_{R,m(s)} I(s\bar{\gamma}^R) \right] \quad (3)$$

For log-detected SAR image, homogenous clutter is predominant when targets occupy small parts, and wavelet coefficients in lowest frequency subband can be modeled as Gaussian distribution [14], so is the distribution of predict residual $w(s)$.

In fact, target areas in predicted residual image are brighter than remains. We now compute a test statistic based on the residual between the predicted coefficient and any given image coefficient as shown in equation

$$\zeta(s) = \frac{w(s) - \mu_c}{\sigma_c} \quad (4)$$

where μ_c is the average of the expected residual for the object model, and σ_c is the standard deviation of those coefficients.

For every scale of residual image, target areas appear much brighter than remains. To make our search criteria for a given object more robust, we build a complicated test statistic

$$c(s) = \left[\zeta(s) + \zeta(s\bar{\gamma}) + \zeta(s\bar{\gamma}^2) + \ldots + \zeta(s\bar{\gamma}^{N-2}) \right] / \sqrt{N-1} \quad (5)$$

where N is wavelet decomposition levels of 4.

When the Gaussian $c(s)$ model is accurate, and the target occupies a small part, threshold $c(s)$ at value of T leads to a per-pixel false alarm probability of

$$P_{FA} = \frac{1}{2} \mathrm{erfc}\left(\frac{T}{\sqrt{2}} \right) \quad (6)$$

Assuming Q independent pixels per square kilometer, the corresponding false alarm rate (FA/km^2) is

$$FAR = \frac{Q}{2}\text{erfc}\left(\frac{T}{\sqrt{2}}\right) \tag{7}$$

To evaluate the performance of $c(s)$ with different wavelet filters, we test it on the public domain MSTAR database. The database contains target and clutter SAR imagery collected at X-band wavelengths. The imagery has a resolution of 1 ft in both the range and azimuth directions. The target data from three different target types BMP2, BTR70, and T72 are divided into a training database of 1622 target chips and a testing database of 1365 chips. The database consists of clutter scenes covering approximately 10 square kilometers of ground. Both the clutter and target data are stored as magnitude detected imagery. Each pixel in the target chip files is stored as binary 4 bytes floating point value, and each pixel in the clutter scene files is stored as binary unsigned short integer. We transform the magnitude image into log-detected image and compute multiresolution detection statistic in wavelet domain both on target chips and clutter scenes, where target multiscale model is built using 64 images imaged at a different aspect angle (extracting 32×32 pixels target chip) from confuser zsu-23-4 training set. Using a broad range of thresholds, clutter scenes have been processed with prescreening algorithm to extract the global FAR. Then, the target testing chips have been processed to estimate the same range of thresholds. We obtain receiver operating characteristic (ROC) curves, which represent the number of detections plotted against the number of false alarms at various threshold setting. Fig. 4 shows ROC curves for different detectors over the public MSTAR database, where "CFAR" is referred to two-parameter CFAR detector in image domain; others are multiresolution CFAR detectors in wavelet domain with different wavelet basis functions. It illustrates performance of $c(s)$ using db4 wavelet outperforms others.

2.4. ROI Mask

Threshold is determined according to the required FAR. Compared multiresolution CFAR value to the threshold, a binary image is formed, and ROI is extracted after morphological processing.

In order to identify the wavelet coefficients belonging to the ROI or to the background, ROI mask is generated. ROI mask will be expanded at each level of decomposition due to filter expansion [15]; this can be seen from the following inverse wavelet transform.

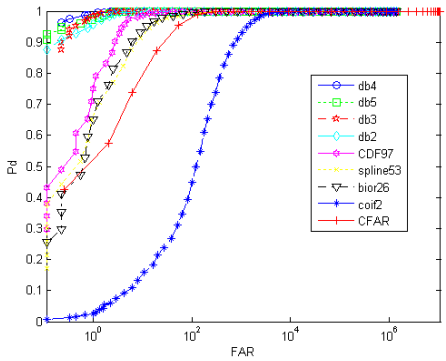

Figure 4. ROC curves over public MSTAR database in log-detected domain.

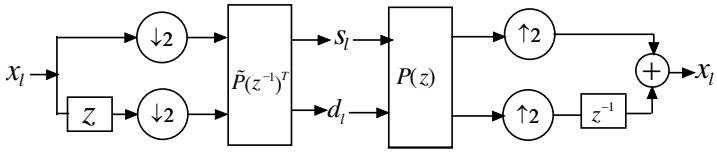

Figure 5. Polyphase representation of wavelet transform.

2.4.1. Factoring db4 Wavelet Transforms into Lifting Steps

Factoring db4 wavelet transforms into lifting steps can be summarized as follows:

1) Polyphase representing db4 synthesis filters h and g, we get synthesis polyphase matrix $P(z)$.

Db4 wavelet is an orthogonal base. Inverse transform uses two synthesis filters h and g. Under the perfect reconstruction condition here we have [16]:

$$h(z) = h_0+h_1z^{-1}+h_2z^{-2}+h_3z^{-3}+h_4z^{-4}+h_5z^{-5}+h_6z^{-6}+h_7z^{-7} \quad (8)$$

$$g(z) = h_7z^6 - h_6z^5 + h_5z^4 - h_4z^3 + h_3z^2 - h_2z^1 + h_1 - h_0z^{-1} \quad (9)$$

Polyphase representation of wavelet transforms can be illustrated schematically in Fig. 5.

Polyphase representation of synthesis filters is given by

$$h(z) = h_e(z^2) + z^{-1}h_o(z^2) \quad (10)$$

$$g(z) = g_e(z^2) + z^{-1}g_o(z^2) \quad (11)$$

where h_e contains the even coefficients, and h_o contains the odd coefficients.

Corresponding synthesis polyphase matrix $P(z)$ is

$$P(z) = \begin{bmatrix} h_e(z) & g_e(z) \\ h_o(z) & g_o(z) \end{bmatrix} = \begin{bmatrix} h_0+h_2z^{-1}+h_4z^{-2}+h_6z^{-3} & h_7z^3+h_5z^2+h_3z+h_1 \\ h_1+h_3z^{-1}+h_5z^{-2}+h_7z^{-3} & -h_6z^3-h_4z^2-h_2z-h_0 \end{bmatrix} \quad (12)$$

2) Using Euclidean algorithm for Laurent polynomial, factor $P(z)$ into lifting steps.

$P(z)$ can be factored into lifting steps

$$P(z) = \begin{pmatrix} 1 & 0 \\ -\alpha & 1 \end{pmatrix} \begin{pmatrix} 1 & -(\beta z^{-1}+\beta') \\ 0 & 1 \end{pmatrix} \begin{pmatrix} 1 & 0 \\ -(\gamma z^{-1}+\gamma') & 1 \end{pmatrix} \begin{pmatrix} 1 & -(\eta z^{-1}+\eta') \\ 0 & 1 \end{pmatrix} \begin{pmatrix} 1 & 0 \\ 1 & 1 \end{pmatrix} \begin{pmatrix} 1 & -1 \\ 0 & 1 \end{pmatrix} \begin{pmatrix} 1 & -(\lambda_3 z^3 + \lambda_2 z^2 + \lambda_1 z + \lambda_0) \\ 0 & 1 \end{pmatrix} \begin{pmatrix} -k_1^{-1} & 0 \\ 0 & k_1 \end{pmatrix} \quad (13)$$

where coefficients are shown in Table 2.

3) Obtain analysis polyphase matrix $\tilde{P}(z^{-1})^T$ lifting steps.

Polyphase matrix $P(z)$ is para-unitary, and the analysis polyphase matrix is factored as

$$\tilde{P}(z^{-1})^T = P(z^{-1})^T = \begin{pmatrix} -k_1^{-1} & 0 \\ 0 & k_1 \end{pmatrix} \begin{pmatrix} 1 & 0 \\ -(\lambda_3 z^{-3}+\lambda_2 z^{-2}+\lambda_1 z^{-1}+\lambda_0) & 1 \end{pmatrix} \begin{pmatrix} 1 & 0 \\ -1 & 1 \end{pmatrix} \begin{pmatrix} 1 & 1 \\ 0 & 1 \end{pmatrix} \begin{pmatrix} 1 & 0 \\ -(\eta z+\eta') & 1 \end{pmatrix} \begin{pmatrix} 1 & -(\gamma z+\gamma') \\ 0 & 1 \end{pmatrix} \begin{pmatrix} 1 & 0 \\ -(\beta z+\beta') & 1 \end{pmatrix} \begin{pmatrix} 1 & -\alpha \\ 0 & 1 \end{pmatrix} \quad (14)$$

Table 2. Coefficients in lifting steps.

k_1	1.362166720130752
λ_0	-1
$\lambda 1$	-0.469083478901698
λ_2	0.140039237726832
λ_3	-0.024791238156143
η	2.131816712755221
γ'	0.117648086798478
γ	-0.018808352726244
β'	-0.300142258748545
β	-1.117123605160594
α	-0.322275887997141

This corresponds to the following implementation for the forward transform:

$$\begin{aligned}
s_l^{(1)} &= x_{2l} - \alpha x_{2l+1} \\
d_l^{(1)} &= -\beta s_{l+1}^{(1)} + \beta' s_l^{(1)} + x_{2l+1} \\
s_l^{(2)} &= s_l^{(1)} - \gamma d_{l+1}^{(1)} - \gamma' d_l^{(1)} \\
d_l^{(2)} &= -\eta s_{l+1}^{(2)} + \eta' s_l^{(2)} + d_l^{(1)} \\
s_l^{(3)} &= s_l^{(2)} + d_l^{(2)} \\
d_l^{(3)} &= -s_l^{(3)} + d_l^{(2)} \\
d_l^{(4)} &= -\lambda_3 s_{l-3}^{(3)} - \lambda_2 s_{l-2}^{(3)} - \lambda_1 s_{l-1}^{(3)} + s_l^{(3)} + d_l^{(3)} \\
s_l &= -k_1^{-1} s_l^{(3)} \\
d_l &= k_1 d_l^{(4)}
\end{aligned} \tag{15}$$

4) Derive the inverse transform from the forward by running the scheme backward.

The inverse transform follows from reversing the operation above:

$$\begin{aligned}
d_l^{(4)} &= k_1^{-1} d_l \\
s_l^{(3)} &= -k_1 s_l \\
d_l^{(3)} &= d_l^{(4)} + \lambda_3 s_{l-3}^{(3)} + \lambda_2 s_{l-2}^{(3)} + \lambda_1 s_{l-1}^{(3)} - s_l^{(3)} \\
d_l^{(2)} &= s_l^{(3)} + d_l^{(3)} \\
s_l^{(2)} &= s_l^{(3)} - d_l^{(2)} \\
d_l^{(1)} &= d_l^{(2)} + \eta s_{l+1}^{(2)} - \eta' s_l^{(2)} \\
s_l^{(1)} &= s_l^{(2)} + \gamma d_{l+1}^{(1)} + \gamma' d_l^{(1)} \\
x_{2l+1} &= d_l^{(1)} + \beta s_{l+1}^{(1)} - \beta' s_l^{(1)} \\
x_{2l} &= s_l^{(1)} + \alpha x_{2l+1}
\end{aligned} \tag{16}$$

where s_l, d_l are smoothed values and details.

2.4.2. Generic ROI Mask

Substituting corresponding equations in (16) into x_{2l} and x_{2l+1}, we have

$$\begin{aligned} x_{2l} &= -0.042440281901326s_{l-3}+0.243472801647206s_{l-2} \\ &\quad -0.826346497388014s_{l-1}-1.334009475194556s_l \\ &\quad +0.071866284832564s_{l+1}-0.070309030395583s_{l+2} \\ &\quad +0.019663459654361s_{l+3}-0.922612876108825d_l \\ &\quad +0.081276337771496d_{l+1}-0.047834398217298d_{l+2} \\ &\quad +0.010597401784553d_{l+3} \qquad (17) \\ x_{2l+1} &= 0.047077471137254s_{l-3}-0.385761392806003s_{l-2} \\ &\quad +1.578703595168067s_{l-1}-1.842525444396078s_l \\ &\quad -1.386321955378261s_{l+1}+0.387638102321498s_{l+2} \\ &\quad -0.061014368082466s_{l+3}+1.023421124931658d_l \\ &\quad -2.605060547408171d_{l+1}+0.239762977284376d_{l+2} \\ &\quad -0.032883011665605d_{l+3} \qquad (18) \end{aligned}$$

From the above expressions, we know that the coefficients necessary to reconstruct $x(2l)$ and $x(2l+1)$ are low frequency subband coefficients $L(l-3)$, $L(l-2)$, $L(l-1)$, $L(l)$, $L(l+1)$, $L(l+2)$, $L(l+3)$ and high frequency subband coefficients $H(l)$, $H(l+1)$, $H(l+2)$, $H(l+3)$, as shown in Fig. 6.

To simplify ROI shape information and alleviate the computation complexity of ROI mask, we specify a rectangular region associated with the designated ROI. Thus, the identified ROI is bounded by a rectangle. For the rectangle, only two positions need be studied, namely the upper left and lower right corners. All samples in between the two corners are considered to belong to the mask. Using the usual

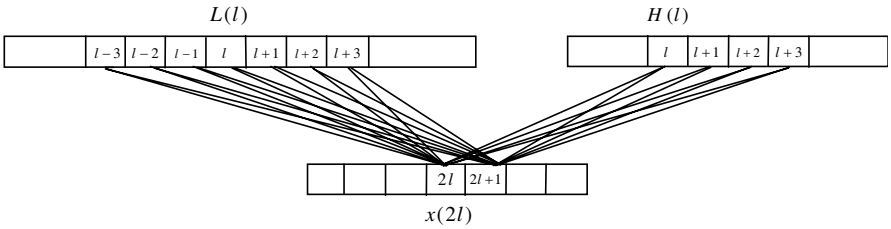

Figure 6. The inverse db4 tansform:the coefficients necessary to reconstruct $x(2l)$ and $x(2l+1)$ are $L(l-3)$ to $L(l+3)$ and $H(l)$ to $H(l+3)$, respectively.

Table 3. ROI mask support.

Generic		Modified	
$lnSup$	3	$lenSup$	2
		$lonSup$	2
$lpSup$	3	$lepSup$	0
		$lopSup$	2
$hnSup$	0	$henSup$	0
		$hepSup$	0
$hpSup$	3	$honSup$	0
		$hopSup$	2

convention that the origin of the subband coordinates occurs at the top-left corner of the subband, the ROI in the parent subband covered the coefficients between (x_0, y_0) and (x_1, y_1), then in the new subband it will cover (x'_0, y'_0) and (x'_1, y'_1), where

$$\begin{aligned} x'_0 &= floor(x_0/2) - nSup, \quad y'_0 = floor(y_0/2) - nSup \\ x'_1 &= floor(x_1/2) + pSup, \quad y'_1 = floor(y_1/2) + pSup \end{aligned} \tag{19}$$

The choice of $nSup$ and $pSup$ will depend on whether the (x'_i, y'_i) $(i = 0, 1)$ is in the low or the high frequency subband. Let constants $lnSup$ (low, negative support), $lpSup$ (low, positive support), $hnSup$ (high, negative support) and $hpSup$ (high, positive support) denote support under the four situations. They are shown in Table 3.

We assume that the ROI mask of subband HL_1, LH_1 and HH_1 is the same as that of subband LL_1.

2.4.3. Modified ROI Mask

Although higher bit rate is given to ROI, coding performance of target area degrades dramatically if we mask significant wavelet coefficient as formula (19). The reason is that the significant coefficients expand too fast even throughout the whole image.

To mitigate the situation above, in analysis expression (17), (18) we note that each item has different effect on the reconstruction. Since the absolute maximum of the weight coefficient is about 2.0 (1.8425254443960), the absolute weighting coefficient value smaller than 0.1 can be negligible compared to it. So we ignore the item whose absolute weighting coefficient is smaller than 0.1, and expression

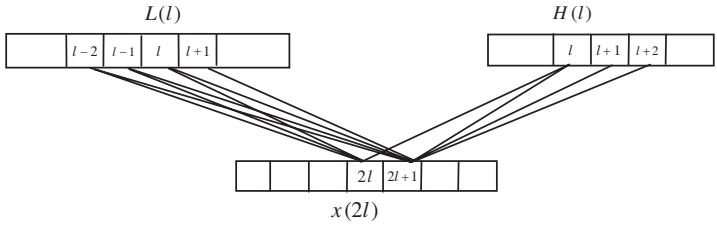

Figure 7. To approximately reconstruct $x(2l)$, the coefficients necessary are $L(l-2)$ to $L(l)$ and $H(l)$; To approximately reconstruct $x(2l+1)$, the coefficients necessary are $L(l-2)$ to $L(l+2)$ and $H(l)$ to $H(l+2)$.

(17), (18) are reformulated:

$$\begin{aligned} x_{2l} \approx\ & 0.243472801647206 s_{l-2} - 0.826346497388014 s_{l-1} \\ & - 1.334009475194556 s_l - 0.922612876108825 d_l \qquad (20) \\ x_{2l+1} \approx\ & - 0.385761392806003 s_{l-2} + 1.578703595168067 s_{l-1} \\ & - 1.842525444396078 s_l - 1.386321955378261 s_{l+1} \\ & + 0.387638102321498 s_{l+2} + 1.023421124931658 d_l \\ & - 2.605060547408171 d_{l+1} + 0.239762977284376 d_{l+2} \qquad (21) \end{aligned}$$

We modify ROI mask formula (19) according to approximate reconstruction expressions (20), (21). The choice of $nSup$, $pSup$ will depend on not only whether (x'_0, y'_0), (x'_1, y'_1) is in the low or high frequency subband but also whether the x_i, y_i $(i = 0, 1)$ value is odd or even. Let constants $lenSup$ (low, even, negative support) etc. denote support under the eight situations. As shown in Table 3, mask support lengths are shrunk after modification.

Now only low frequency subband coefficients from $L(l-2)$ to $L(l)$ and high subband coefficients $H(l)$ are needed to approximately reconstruct $x(2l)$, but low frequency subband coefficients from $L(l-2)$ to $L(l+2)$ and high subband coefficients from $H(l)$ to $H(l+2)$ are needed to approximately reconstruct $x(2l+1)$, as show in Fig. 7.

2.5. Rate Allocation

The overall bit rates in bits per pixel for the targets and for the background are either provided by the user or determined by some automated means. Given R_1 bpp for the target and R_2 bpp for

background, rate allocation procedure can be used to allocate rate in rate-distortion optimization sense for target and background sequences separately.

For target sequences, the rate allocation procedure is summarized as follows:

1) Initial λ_l and λ_h, set the bound of bisection research for λ.

2) Computation $\lambda = \frac{\lambda_l + \lambda_h}{2}$.

3) Chosen rate allocation vector $T = (t_1, t_2, \ldots, t_M)$, so that $\min \sum_{i=1}^{M} (\alpha_i \sigma_i^2 E_i(t_i) + \lambda \alpha_i t_i)$, where σ_i^2 is the variance of sequence i, and $E_i(t_i)$ denotes the rate-distortion performance at t_i bits/sample. M is the number of data sequences (that is 22), and α_i is a weighting coefficient to account for variability in sequence length.

4) Computation $T' = \sum_{i=1}^{M} \alpha_i t_i$. If $T' > R_1$, set $\lambda_l = \lambda$; if $T' < R_1$, set $\lambda_h = \lambda$; jump to (2).

Rate allocation for background sequences is similar to the target sequence, only minor modification needed: R_1 in step (4) must be modified as R_2.

3. RESULTS

To illustrate the performance of target-aided image intelligent compression algorithm, we do experiments on $HB03787.001$ from BMP2 training set and $HB03397.015$ from T72 testing set in MSTAR data base. Fig. 8(a) and Fig. 9(a) show their log-detected images, both of original magnitude images are 16 bpp. We use a multiresolution CFAR threshold of 3.84 [17]. Fig. 8(b) and Fig. 9(b) show ROI extracted and their mask. Studies previously have shown that SAR

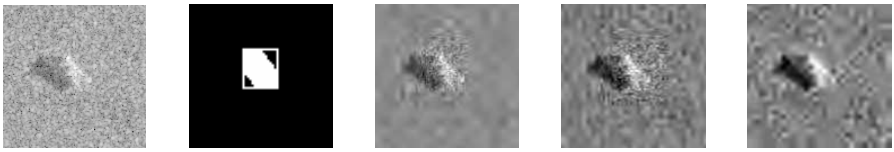

(a) (b) (c) (d) (e)

Figure 8. (a) HB03787.001. (b) ROI and its mask. (c) TAIC with modified ROI mask (0.135 bpp, 2 bpp for target area). (d) TAIC with generic ROI mask (0.137 bpp, 2 bpp for target area). (e) JPEG2000 algorithm (0.14 bpp).

imagery can be compressed by 4 : 1 to 8 : 1 without significantly degrading ATR performance [18]. So we give a larger bit rate of target area from 8 bpp to 2 bpp at step 1 bpp, very low bit rate only of 0.01 bpp to background data [19] in order to achieve large compression. We evaluate compression system performance by SNR's of target area (pixels corresponding to rectangular area), which is defined in (22). Performance results are included in Tables 4 and 5 at different bit rates. For comparison, the performance results of JPEG2000 algorithm are also included. As verified in two tables, TAIC algorithm shows exceptional target area coding efficiency, and modified ROI mask enhances the performance.

$$SNR = 10\log_{10}\left(\frac{\sum_{i=1}^{M}\sum_{j=1}^{N} g(i,j)^2}{\sum_{i=1}^{M}\sum_{j=1}^{N}[g(i,j)-h(i,j)]^2}\right) \tag{22}$$

where $g(i,j)$ is pixel value at site (i,j) in log-magnitude image, $h(i,j)$ is accordingly decoded value, M and N are the dimensions of the image.

Figures 8(c), 9(c) show how TAIC algorithm using modified ROI mask performs, and Figs. 8(d), 9(d) show how the TAIC algorithm using generic ROI mask performs. Figures 8(e), 9(e) show the performance of JPEG2000 algorithm. All of them are working at compression ratio 100 (bit rate for target area is 2 bpp). From these figures, we know TAIC algorithm with modified ROI mask outperforms that with generic ROI mask, and either of them performs better than JPEG2k algorithm. Context information (shadow) is preserved, which is useful for ATR [20].

The computational complexity of proposed algorithm is mainly determined by the size of image and target. We decompose the image

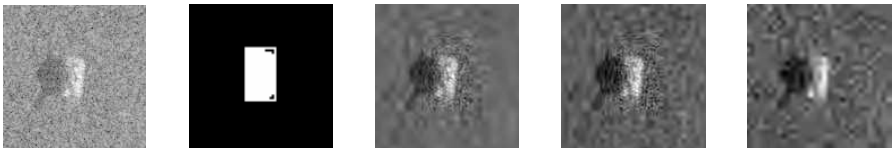

(a) (b) (c) (d) (e)

Figure 9. (a) HB03397.015. (b) ROI and its mask. (c) TAIC with modified ROI mask (0.153 bpp, 2 bpp for target area). (d) TAIC with generic ROI mask (0.159 bpp, 2 bpp for target area). (e) JPEG2000 algorithm (0.14 bpp).

Table 4. SNR of target area comparing our TAIC algorithm and JPEG2000 compression algorithm for HB03787.001.

bpp	TAIC		JPEG2000
	Modified ROI	Generic ROI	
0.15	35.78 (dB)	32.07 (dB)	27.40 (dB)
0.20	40.72 (dB)	34.70 (dB)	27.99 (dB)
0.25	44.52 (dB)	37.50 (dB)	28.45 (dB)
0.30	47.63 (dB)	40.89 (dB)	28.99 (dB)
0.40	49.16 (dB)	44.36 (dB)	29.92 (dB)

Table 5. SNR of target area comparing our TAIC algorithm and JPEG2000 compression algorithm for HB03397.015.

bpp	TAIC		JPEG2000
	Modified ROI	Generic ROI	
0.15	32.35 (dB)	30.01 (dB)	23.97 (dB)
0.20	37.51 (dB)	34.00 (dB)	25.11 (dB)
0.30	43.47 (dB)	37.00 (dB)	26.90 (dB)
0.40	47.00 (dB)	41.00 (dB)	28.08 (dB)

up to 4 levels. Multiresolution target detection algorithm in wavelet domain is much simpler than two-parameter CFAR detection algorithm in image domain. ROI mask generation is simple too. The robust quantizer is only used to encode target sequences and leads to a much less complex implementation since targets only occupy small parts of SAR image. The number of admissible quantizers for each sequence is also a small constant compared to the size of image. Furthermore, the number of iterations for bisection search of a convex curve is relatively small. Therefore, the total computational complexity of our algorithm is $O(MN)$ for an image of size $M \times N$.

4. CONCLUSION

We have investigated a target-aided SAR image intelligent compression system with a multiresolution target detection scheme to designate ROIs, where ROIs are encoded with robust FRTCQ, and the remains are encoded with FRTCQ. We have found that multiresolution CFAR detector using db4 wavelet is more reliable than others. We create generic ROI mask according to the lifting steps of db4 wavelet inverse

transform. To ameliorate the situation that significance coefficients expand too fast, which results in that the coding performance of target area degrades dramatically, we modified ROI mask with respect to the expression of the inverse wavelet transform. As coding results illustrate, TAIC algorithm performs better than JPEG2k algorithm, and modified ROI mask enhances the target area coding efficiency. The image coder enables the transmission of very-high-quality compressed imagery over limited bandwidth noisy channels without need for entropy coding and its associated complexity and susceptibility to channel errors. The robust quantizer is only used to encode target sequences which leads to a much less complex implementation since targets occupy small parts of SAR image.

REFERENCES

1. Chan, Y. K. and V. C. Koo, "An introduction to Synthetic Aperture Radar (SAR)," *Progress In Electromagnetics Research B*, Vol. 2, 27–60, 2008.
2. Li, N.-J., C.-F. Hu, L.-X. Zhang, and J.-D. Xu, "Overview of RCS extrapolation techniques to aircraft targets," *Progress In Electromagnetics Research B*, Vol. 9, 249–262, 2008.
3. Zou, B., H. Cai, L. Zhang, and M. Lin, "Model of man-made target beneath foliage using polinsar," *Progress In Electromagnetics Research Letters*, Vol. 2, 21–28, 2008.
4. Xue, W. and X.-W. Sun, "Target detection of vehicle volume detecting radar based on wigner-hough transform," *Journal of Electromagnetic Waves and Applications*, Vol. 21, No. 11, 1513–1523, 2007.
5. Lee, J. H. and H. T. Kim, "Radar target discrimination using transient response reconstruction," *Journal of Electromagnetic Waves and Applications*, Vol. 19, No. 5, 655–669, 2005.
6. Jung, J. H., H. T. Kim, and K. T. Kim, "Comparisons of four feature extraction approaches based on Fisher's linear discriminant criterion in radar target recognition," *Journal of Electromagnetic Waves and Applications*, Vol. 21, No. 2, 251–265, 2007.
7. Seo, D.-K., K. T. Kim, I. S. Choi, and H. T. Kim, "Wide-angle radar target recognition with subclass concept," *Progress In Electromagnetics Research*, PIER 44, 231–248, 2004.
8. Alan, C., M. Kristo, L. Austin, and L. Margaret, "A compression of detected SAR imagery with JPEG2000," *SPIE*, Vol. 4115, 510–520, 2000.

9. Zhang, J., Y. Huang, and H. Tian, "SAR image compression based on image decomposing and targets extracting," *1st Asian and Pacific Conference on Synthetic Aperture Radar Proceedings*, 671–673, 2007.
10. Venkatraman, M., H. Kwon, and N. M. Nasrabadi, "Object-based SAR image compression using vector quantization," *IEEE Transactions on Aerospace and Electronic Systems*, Vol. 36, No. 4, 1036–1046, 2000.
11. Bonneau, R. and G. Abousleman, "Target-aided fixed-quality-of-service compression of SAR imagery for transmission over noisy wireless channels," *ICASSP'02*, Vol. 4, IV-3413–IV-3416, 2002.
12. Tanabe, N. and N. Farvardin, "Subband image coding using entropy coded quantization over noisy channels," *IEEE Journal Select. Areas Commun.*, Vol. 10, 926–942, 1992.
13. Abousleman, G. P., "Wavelet-based hyperspectral image coding using robust fixed-rate trellis-coded quantization," *SPIE*, Vol. 3372, 74–85, 1998.
14. Birney, K. and T. Fishcher, "On the modeling of DCT and subband image data for compression," *IEEE Transactions on Image Processing*, Vol. 4, No. 2, 186–193, 1995.
15. Park, K.-H. and H. W. Park, "Region-of-interest coding based on set partioning in hierarchical trees," *IEEE Transaction on Circuits and Systems for Video Technology*, Vol. 12, No. 2, 106–113, 2002.
16. Daubechies, I. and W. Sweldens, "Factoring wavelet transforms into lifting steps," *The Journal of Fourier Analysis and Applications*, Vol. 4, No. 3, 247–269, 1998.
17. Novak, L. and S. Owirka, "Effects of polarization and resolution on SAR ATR," *IEEE Transactions on Aerospace and Electronic Systems*, Vol. 33, No. 1, 102–116, 1997.
18. Gorman, J. D., "Assessing the impact of image compression on SAR automatic target detection and cueing," *Radar Conference*, 118–123, 1996.
19. Kim, A. and H. Krim, "Hierarchical stochastic modeling of SAR imagery for segmentation/compression," *IEEE Transaction on Signal Processing*, Vol. 47, No. 2, 458–468, 1999.
20. Lombardom, P., M. Sciotti, and L. M. Kaplan, "SAR prescreening using both target and shadow information," *IEEE Radar Conference*, 147–152, Atlanta, USA, 2001.